Nano Research 2015, 8(6): 2024–2032
DOI 10.1007/s12274-015-0714-1
Research Article

ISSN 1998-0124
CN 11-5974/O4

Freestanding macroscopic metal-oxide nanotube films derived from carbon nanotube film templates

He Ma, Yang Wei (✉), Jiangtao Wang, Xiaoyang Lin, Wenyun Wu, Yang Wu, Ling Zhang, Peng Liu, Jiaping Wang, Qunqing Li, Shoushan Fan, and Kaili Jiang (✉)

State Key Laboratory of Low-Dimensional Quantum Physics, Department of Physics & Tsinghua–Foxconn Nanotechnology Research Center, Tsinghua University, Beijing 100084, China

Received: 13 November 2014
Revised: 22 December 2014
Accepted: 3 January 2015

KEYWORDS
metal-oxide nanotube film, atomic layer deposition, carbon nanotube, humidity sensor, catalyst support

ABSTRACT

Aligned carbon nanotube films coated with amorphous carbon were developed into novel templates by atomic layer deposition. Freestanding macroscopic metal-oxide nanotube films were then successfully synthesized by using these templates. The reactive amorphous carbon layer greatly improved the nuclei density, which ensured the high quality of the films and allowed for precise control of the wall thickness of the nanotubes. Using template-synthesized alumina nanotube films, we demonstrate a humidity sensor with a high response speed, a transmission electron microscopy (TEM) grid, and a catalyst support. The cross-stacked assembly, ultrathin thickness, chemical inertness, and high thermal stability of the alumina nanotube films contributed to the excellent performance of these devices. In addition, it is expected that the metal-oxide nanotube films would have significant potential owing to their material richness, macroscopic appearance, flexibility, compatibility with the semiconducting technologies, and the feasibility of mass production.

1 Introduction

Metal-oxide nanotubes have attracted much attention owing to their potential applications in environmental protection [1], green energy [2–4], sensors [5, 6], and so on. Various approaches have been developed for preparing metal-oxide nanotubes, such as the hydrothermal method [7], chemical vapor deposition [8], physical vapor deposition [9], the anodic oxidation method [10, 11], etc.

The template-assisted atomic layer deposition (ALD) technique is one of the most attractive methods for fabricating metal-oxide nanotubes. One-dimensional nanomaterials are used as templates for the further core–shell ALD processes. The ALD shells become the metal-oxide nanotubes after the nanoscale cores are removed. This method is attractive owing to the merits of ALD, including its wide application in synthesizing various metal oxides, the ability to control the deposition thickness, and conformal coating [12–14].

Address correspondence to Yang Wei, WeiYang@tsinghua.edu.cn; Kaili Jiang, JiangKL@tsinghua.edu.cn

Therefore, a variety of metal-oxide nanotubes such as TiO_2, Al_2O_3, ZrO_2, etc. have been synthesized to take advantage of the conformal coating feature of ALD [15–21]. However, because the templates and resulting as-fabricated raw materials are disordered networks, obstacles remain on how to assemble the metal-oxide nanotubes together to meet the requirements of actual devices [22, 23]. Also, powders and such materials are not compatible with conventional thin-film processes. Therefore, it is still necessary to explore new templates in order to realize the preparation of ordered metal-oxide nanotube films.

Here we show that freestanding aligned carbon nanotube (CNT) films drawn from CNT arrays can serve as potential ALD templates for metal-oxide nanotube preparation. High-quality macroscopic, flexible, and aligned metal-oxide nanotube films (Al_2O_3, TiO_2, HfO_2, etc.) were successfully fabricated using amorphous carbon (AC)-coated cross-stacked CNT films as templates because the amorphous carbon effectively improves the nuclei density of the ALD process. Using Al_2O_3 nanotube freestanding films, we demonstrate a humidity sensor with a high response speed, a grid for transmission electron microscopy (TEM) observation, and a catalyst support. Furthermore, additional applications of metal-oxide freestanding films are expected owing to the macroscopic, flexible, and aligned morphology of the metal-oxide films and their rich functionality.

2 Results and discussion

The aligned CNT films were drawn from super-aligned CNT (SACNT) arrays grown on 8 in. Si wafers. Two layers of CNT films were cross stacked on 24 mm × 24 mm metal frames (Fig. 1(a)) [24]. The cross-stacked structure of the aligned CNT films is shown in Fig. 1(b). An amorphous carbon (AC) layer, 2 nm in thickness, was then coated on the cross-stacked CNT film to serve as a reactive nuclei layer for the ALD process. Figure 1(f) shows a conformal AC sheath surrounding a CNT (AC–CNT). Metal-oxide layers were then deposited on the AC–CNT films by ALD. Figure 1(c) shows an alumina-coated CNT film after 210 ALD cycles. The obvious changes in the transparency and color of the film show successful alumina deposition. Further experiments revealed that the alumina layers coaxially coated on the AC–CNTs were uniform and had smooth surfaces, as shown in Fig. 1(e). Thus it can be concluded an ideal core–shell structure, as sketched in Fig. 1(d), was made. Freestanding alumina nanotube (ANT) films were successfully fabricated after the carbon cores were removed from the core–shell structures by annealing in air at 650 ℃ for 1 h, as shown in Figs. 1(g)–1(j). The SEM image (Fig. 1(h)) shows that the ANT film cloned the cross-stacked structure from the templates. Figure 1(j) shows the TEM image of an ANT in the as-fabricated film and selected-area electron diffraction (SAED) shows that the alumina of the

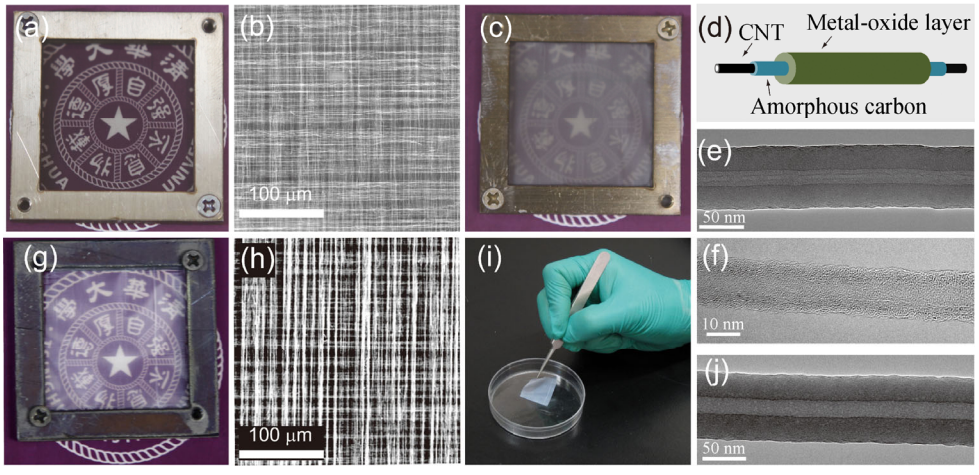

Figure 1 (a) Photograph of a cross-stacked CNT film. (b) SEM image of a cross-stacked CNT film. (c) An AC–CNT film after coating alumina with 210 ALD cycles. (d) Sketch of the alumina-coated AC–CNT. (e) TEM image of an AC–CNT coated with 210-ALD-cycle alumina coaxially. (f) TEM image of an AC–CNT. (g) ANT-210 film after removing the CNTs. (h) SEM image of an ANT-210 film. (i) ANT-210 film detached from the metal frame. (j) TEM image of the ANT in the ANT-210 film.

nanotube was amorphous (Fig. S1 in the Electronic Supplementary Material (ESM)). The ANT film was robust, such that it could be detached from the frame, and it was also flexible, as shown in Fig. 1(i).

Coating the CNT films with amorphous carbon is necessary for preparing a high-quality metal-oxide nanotube film. Figures 2(a)–2(c) show TEM images of pristine SACNTs coated by 70, 140, and 210 ALD cycles of alumina, respectively. In the case of 70 ALD cycles, isolated alumina nanoparticles grew on the CNTs. Increasing the number of ALD cycles to 140 and 210 resulted in larger alumina nanoparticles that coalesced gradually. Only rough alumina layers could be synthesized on the pristine CNTs, even with multiple ALD cycles, and the resulting alumina shells retained that rough morphology (Figs. 2(e)–2(g)). Marichy et al. [25] reported that metal oxides prefer to grow on defects on CNT surfaces. When the surfaces have a high defect density, the metal oxide can be coated onto the CNTs conformally. Otherwise, the metal oxide grows on the CNTs as islands. Therefore, on the basis of our experiments and the fact that SACNTs have clean surfaces without dangling bonds [26], pristine SACNTs present an unreactive surface for ALD precursors, resulting in the island growth mode [25, 27], as schematically illustrated in Fig. 2(d). Alumina can only nucleate at a few defects on the SACNTs initially. The size of the nuclei increases with increasing ALD cycles. Neighboring alumina nanoparticles begin to overlap, eventually reducing the surface roughness. An amorphous carbon layer was thus introduced to increase the nuclei density and improve the quality of the metal-oxide nanotubes. We also note that many methods, including covalent and non-covalent surface functionalization, have been developed to realize coaxial coating of metal oxides on CNTs by ALD [28–32]. However, amorphous carbon decoration introduced by magnetron sputtering is a satisfactory choice for SACNT films because it is compatible with conventional thin-film processes and can avoid destruction of the freestanding SACNT films.

The number of defects and functional groups on the SACNT films significantly increased after the introduction of the amorphous carbon. Figure 3(a) shows the Raman spectra of pristine CNTs and AC–CNTs. The ratios of I_D to I_G are 0.83 and 1.15, respectively, which is indicative of an apparent increase in the number of defects. Fourier transform infrared spectroscopy (FTIR) was performed to further identify functional groups introduced by the amorphous carbon. After the amorphous carbon-coating process, the peak at 1,160 cm^{-1} (C–O bond [33]) is significantly enhanced and the peak at 1,724 cm^{-1} (C=O bond [33]) is sharper. Therefore, the newly introduced defects, i.e., the C–O and C=O bonds, contributed to improving the nuclei density on the ALD templates and thus played an important role during the alumina nucleation.

By introducing the amorphous carbon reactive layer, we were able to fabricate freestanding ANT films with thinner walls. Figures 3(c)–3(f) show the morphologies

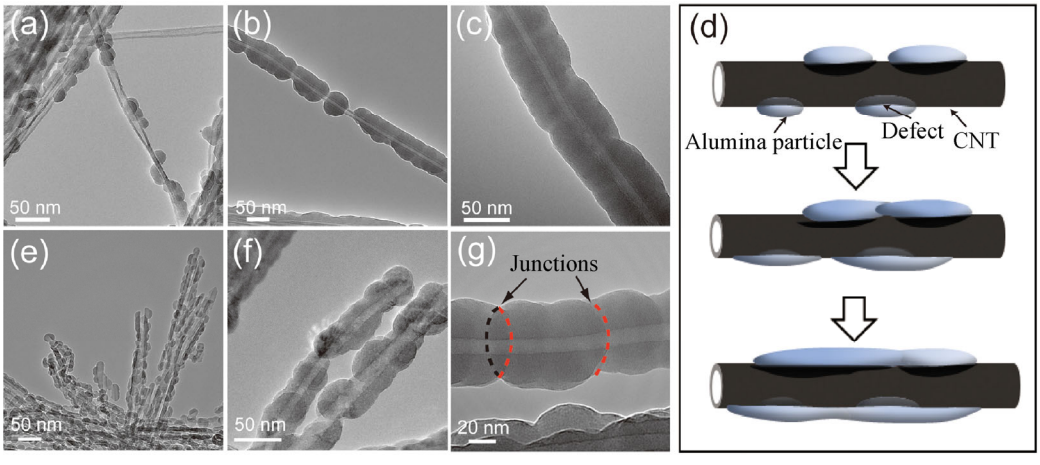

Figure 2 Morphologies of alumina-coated pristine CNTs by (a) 70, (b) 140, and (c) 210 ALD cycles. (d) Sketch of the metal-oxide deposition with low nuclei density. Morphologies of alumina shells obtained by (e) 70, (f) 140, and (g) 210 ALD cycles after removing CNT cores.

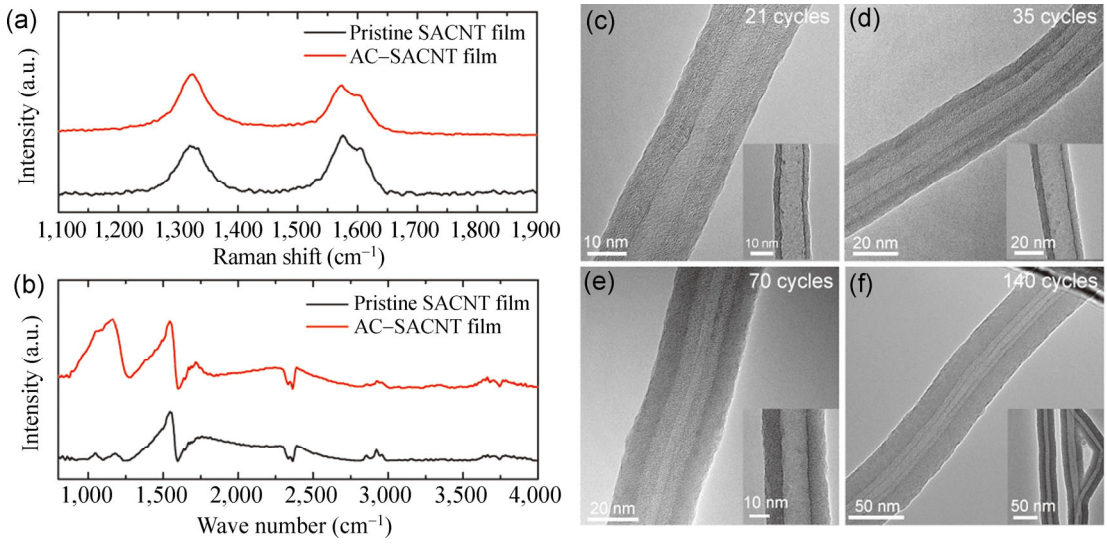

Figure 3 (a) Raman spectra of the pristine CNT film and the AC–CNT film. (b) FTIR spectra of the pristine CNT film and the AC–CNT film. Alumina coated on AC–CNTs by (c) 21, (d) 35, (e) 70, and (f) 140 ALD cycles. The insets are the corresponding ANTs after removing the AC–CNT cores.

of the alumina shells on AC–CNTs deposited by 21, 35, 70, and 140 ALD cycles, respectively. The corresponding ANTs with different wall thickness are shown in the insets. The thinnest ANT wall was 3 nm (21 ALD cycles). The wall thickness versus the number of ALD cycles is plotted in Fig. 4(a). The slope of the curve gives an approximate growth rate of 0.13 nm per ALD cycle. These results indicate that the wall thickness of ANTs can be controlled precisely by the controlling the number of ALD cycles.

The physical properties of the ANT films can be regulated by controlling the wall thickness. We studied the wall-thickness-dependent transmittances and mechanical properties. The optical transmittances of the ANT-35, ANT-70, ANT-140, and ANT-210 films at 550 nm, shown in Fig. 4(b), are 99%, 91%, 67%, and 41%, respectively (the numbers in the specimen names indicate the corresponding number of ALD cycles). Because of the high transparency of the ANT-35 and the ANT-70 films, Chinese characters under them can be seen very clearly (inset of Fig. 4(b)). Weaker scattering and absorbability from ANT films with smaller-diameter NTs (i.e., thinner walls) possibly contributed to the higher transparencies. By increasing the tube diameter, the ANT films became more robust. The maximum tensile loads that 6-mm-wide films could sustain were 14, 43, and 61 mN for ANT-70, ANT-140, and ANT-210, respectively (Fig. 4(c)). However, the maximum tensile load afforded by the ANT film derived from the 210-ALD-cycle alumina on

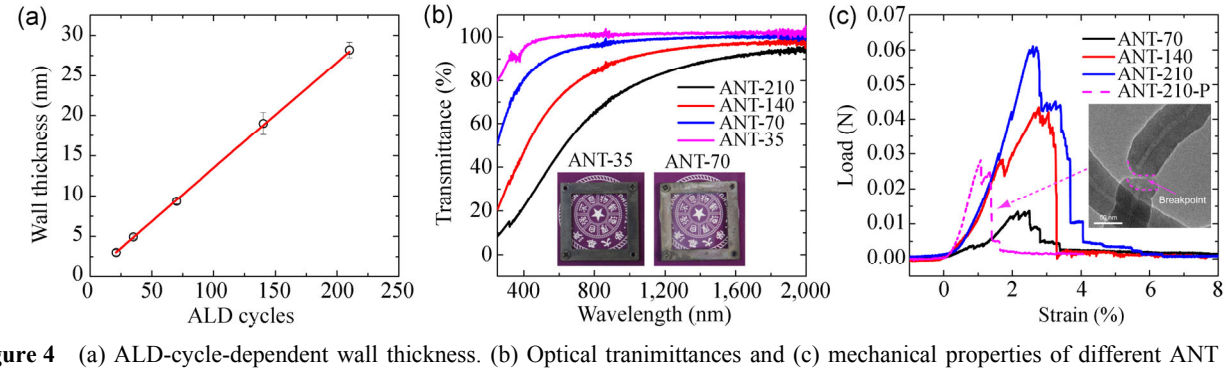

Figure 4 (a) ALD-cycle-dependent wall thickness. (b) Optical tranimittances and (c) mechanical properties of different ANT films. The insets in (b) are photographs of ANT-35 and ANT-70, respectively. The inset in (c) is a TEM image of the breakpoint in the ANT-210-P film after tensile test.

the pristine CNT film (ANT-210-P) was only 29 mN, which is 2.3 times lower than that of ANT-210. In the ANT-210-P film, even though the tubular structure of alumina was formed, the coalescence of alumina nanoparticles could still be traced on the ANTs. The junctions of alumina nanoparticles are marked in Fig. 2(g). These junctions serve as weak joints, and thus significantly affect the mechanical strength. We examined the fracture properties of the ANT-210-P film by TEM after the tensile test. Many breakpoints were found at the junctions of ANTs (inset of Fig. 4(c)), which supports this hypothesis. Moreover, the mechanical experiments further validated the importance of the amorphous carbon reactive layer deposited on the SACNT films for obtaining robust metal-oxide films.

The technique can possibly be developed to mass produce a variety of metal-oxide nanotube films. Besides ANT films, we also fabricated TiO_2 and HfO_2 nanotube films. Figures 5(a) and 5(c) show the freestanding and flexible TiO_2 and HfO_2 nanotube films, respectively. The corresponding TEM images of the nanotubes are shown in Figs. 5(b) and 5(d), respectively. It is also possible to fabricate other types of metal-oxide nanotube films because conventional ALD is a powerful technique for metal-oxide film deposition. Moreover, the production of SACNT arrays and aligned CNT films has been industrialized [34]. It is thus possible to mass produce metal-oxide nanotube films by using AC–CNT templates. These advantages provide a good foundation for further applications.

On the basis of the current progress on ANT film fabrication and the fact that the conductivity of the alumina films is sensitive to water vapor [23, 35], we developed a humidity sensor using the as-prepared ANT film as the functional material. The sensor structure is sketched in the inset of Fig. 6(a). A piece of ANT-210 film (12 mm × 12 mm) was sandwiched between copper foil and a cross-stacked CNT film. A 5 V DC bias was applied between the copper foil and the CNT film. The electric current through the ANT film depended on the humidity of the experiment chamber, as shown in Fig. 6(a). The current increased with increasing humidity, and it was more sensitive when the humidity was higher than 45%. The humidity response is due to the absorbance of water molecules on the ANTs and the formation of conductive channels [23, 35]. The time-response performance of the sensor was further studied by blowing the sensor with

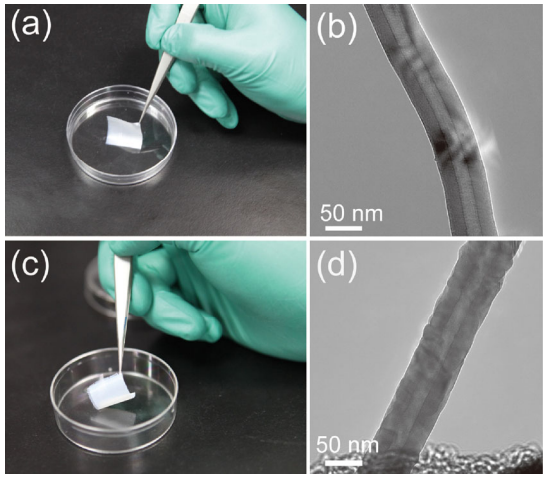

Figure 5 (a) Photograph of a TiO_2 nanotube film. (b) TEM image of a typical TiO_2 nanotube made by 600 ALD cycles. (c) Photograph of an HfO_2 nanotube film. (d) TEM image of an HfO_2 nanotube.

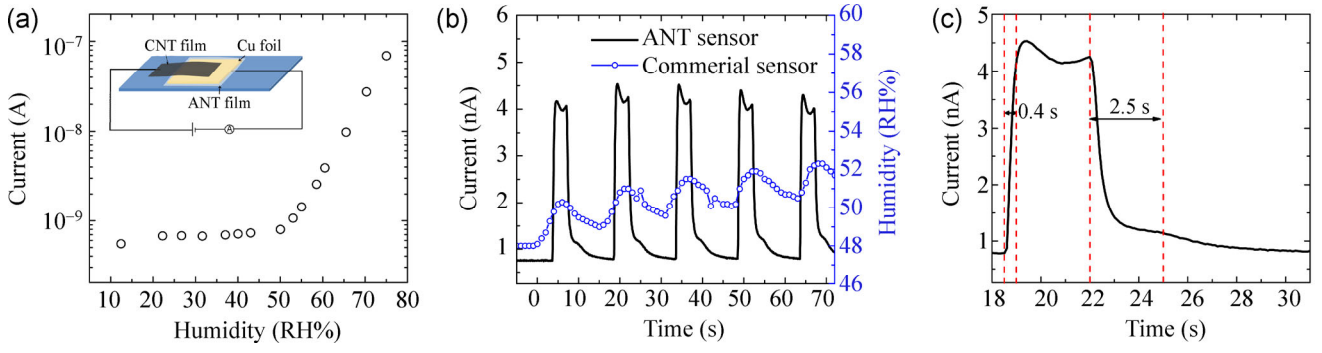

Figure 6 (a) Dependence of current of the ANT humidity sensor on humidity. The inset is a schematic of the ANT humidity sensor. (b) Response of the ANT humidity sensor and a commercial sensor to humid air flow. (c) The response of the ANT humidity sensor to a single pulse of humid air flow.

humidity-modulated air. More experimental details can be found in the supporting materials (Fig. S2 in the ESM). As shown in Fig. 6(b), the ANT humidity sensor responded to the humid flow pulses with sharp current responses, but the reference commercial humidity sensor was much less sensitive. The response and recovery time of the ANT humidity sensor were approximately 0.5 and 2.5 s, respectively (Fig. 6(c)). The fast response of the ANT humidity sensor can be attributed to the ultrathin walls and the high porosity of the ANT films.

ANT films can also be applied as supporting films for TEM observations because the films have numerous nanosized holes, effective edges, and strong absorbability for nanoparticles. The fabrication process, SEM image, and energy dispersive spectroscopy of ANT-TEM grids can be found in the supporting materials (Fig. S3 in the ESM). Au nanoparticles dispersed in water were well dispersed on the ANTs (Fig. 7(a)) owing to the hydrophilicity of alumina. The lattice fringes of the Au nanoparticles are observed clearly at high magnification, indicating that the cross-stacked ANT films have good mechanical stability and can be used to acquire high-resolution, high-quality TEM images. Moreover, the ANT-TEM grids do not contain carbon, and so they are suitable for analyzing the carbon content in samples by energy dispersive spectroscopy (Fig. S3 in the ESM).

The ANT film was further used as a catalyst support. It is known that alumina ceramics are a widely used catalyst support because of their chemical inertness and high thermal stability [13, 36]. The as-prepared ANT film is an ideal catalyst support as it has a large surface area and good permeability as compared to conventional supports. Moreover, the high transparency of the ANT film could have special advantages in the photoelectrochemical field. CNT growth catalyzed by iron nanoparticles is taken as an example to prove the advantage of ANT films as catalyst supports. Owing to numerous nanosized holes and effective edges in the ANT film, we were able to easily find and observe iron nanoparticles on the ANTs under TEM. Figure 7(c) shows many iron nanoparticle catalysts on the ANTs. As seen in the enlarged image (inset in Fig. 7(c)), we observed an iron catalyst surrounded by amorphous carbon, resulting in failure of the iron nanoparticle to catalyze CNT growth. Figure 7(d), on the other hand,

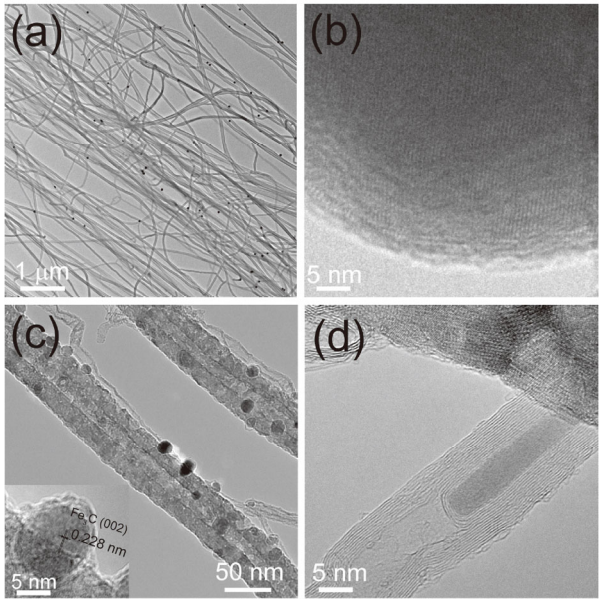

Figure 7 (a) Au nanoparticles dispersed on the ANT-TEM grid. (b) High-resolution TEM image of an Au nanoparticle. (c) Iron catalysts on the ANTs. The insert is an iron particle. (d) A multi-walled CNT grown from a catalyst.

shows a multiwalled CNT successfully grown from the catalyst without damaging the ANT support. The growth mode is bottom-growth because the catalyst is still attached to the ANT support. This reveals the good absorbability of the catalyst on the support, which can effectively prevent catalyst aggregation and loss. Thus the ANT films are potential catalyst supports.

3 Conclusions

In summary, we developed freestanding, flexible, metal-oxide nanotube films with cross-stacked alignment by using AC–CNT films as ALD templates. The reactive amorphous carbon layer greatly improved the nuclei density, thus ensuring the fabrication of high quality metal-oxide films. The as-fabricated ANT films were applied as a humidity sensor with a high response speed, a grid for TEM observations, and a catalyst support for CNT growth. The performance of the films in these applications can be attributed to the special characteristics of the ANT films, such as the cross-stacked assembly, ultrathin NT walls, chemical inertness, high thermal stability, and so on. The metal-oxide

nanotube films have significant potential because of their rich functions, macroscopic flexible appearance, compatibility with thin-film technologies, and the feasibility of mass production.

4 Experimental

Fabrication of AC–CNT films: The preparation of cross-stacked CNT films was the same as that described in our previous work [24]. Briefly, an aligned CNT film was drawn out from an SACNT array and coated on a stainless steel frame. A second CNT film was stacked on the first CNT film in a perpendicular direction. Amorphous carbon deposition on the cross-stacked CNT films was carried out in a magnetron sputtering system with a background vacuum of 2.5×10^{-3} Pa. The sputtering pressure, power, and time were 0.1 Pa, 80 W, and 5 min, respectively.

Coating metal-oxide shells on the templates by ALD: Trimethylaluminium (TMA), titanium tetrachloride (TTC), and tetrakis(ethylmethylamino)hafnium (TEMAH) were used as metal precursors for the synthesis of Al_2O_3, TiO_2, and HfO_2 layers on the SACNT films, respectively. H_2O and N_2 gas were used as the oxygen source and the carrier gas, respectively, in all cases. Coating of Al_2O_3 was performed in a commercial ALD system (NorthStar™, SVTA, USA) at a temperature of 120 °C. One ALD cycle consisted of a 0.02 s exposure to TMA, 25 s of pumping, a 0.01 s exposure to H_2O, and 50 s of pumping. The flow rate of the carrier gas was maintained at 5 sccm. However, coating TiO_2 and HfO_2 were performed in another ALD system (TFS200, Beneq) at temperature of 200 °C. One ALD cycle for TiO_2 consisted of a 0.25 s exposure to TTC, 1 s of pumping, a 0.25 s exposure to H_2O, and 1 s of pumping. The flow rate of the carrier gas was maintained at 200 sccm. One ALD cycle for HfO_2 consisted of a 0.5 s exposure to TEMAH, 2 s of pumping, a 0.25 s exposure to H_2O, and 1 s of pumping. The flow rate of the carrier gas was maintained at 200 sccm.

Physical characterization: The as-prepared metal-oxide films were observed by SEM (Sirion 200, FEI) and TEM (Tecnai F20, FEI). The accelerating voltage for TEM observation was 200 kV. Raman spectra and FTIR spectra measurements were performed by a Raman spectrometer (LabRAM HR800, Jobin Yvon) and FTIR spectrometer (VERTEX 70/70v, Bruker), respectively. The optical and mechanical properties of the ANT films were measured by the PerkinElmer Lambda 950 (ultraviolet–visible–near infrared) spectrometer and the Instron 5848 MicroTester, respectively. The size of the ANT films for the mechanical tests was 10 mm in length and 6 mm in width.

Acknowledgements

This work was supported by the National Basic Research Program of China (No. 2012CB932301), the National Natural Science Foundation of China (Nos. 51472142, 51102147, and 51102144), and the Chinese Postdoctoral Science Foundation (Nos. 2014M550701 and 2012M520261).

Electronic Supplementary Material: Supplementary material (SAED pattern of ANT-140, experimental setup for humidity test, SEM image and EDS of ANT-TEM grids, and growth condition of CNTs on the ANT film) is available in the online version of this article at http://dx.doi.org/10.1007/s12274-015-0714-1.

References

[1] Wang, M. Y; Ioccozia, J.; Sun, L.; Lin, C. J.; Lin Z. Q. Inorganic-modified semiconductor TiO_2 nanotube arrays for photocatalysis. *Energ. Environ. Sci.* **2014**, *7*, 2182–2202.

[2] Favors, Z.; Wang, W.; Bay, H. H.; George, A.; Ozkan, M.; Ozkan, C. S. Stable cycling of SiO_2 nanotubes as high-performance anodes for lithium-ion batteries. *Sci. Rep.* **2014**, *4*, 4605–4612.

[3] Mor, G. K.; Shankar, K.; Paulose, M.; Varghese, O. K.; Grimes, C. A. Use of highly-ordered TiO_2 nanotube arrays in dye-sensitized solar cells. *Nano Lett.* **2005**, *6*, 215–218.

[4] Hwang, Y. J.; Hahn, C.; Liu, B.; Yang, P. D. Photoelectrochemical properties of TiO_2 nanowire arrays: A study of the dependence on length and atomic layer deposition coating. *ACS Nano* **2012**, *6*, 5060–5069.

[5] Zheng, Q.; Zhou, B. X.; Bai, J.; Li, L. H.; Jin, Z. J.; Zhang, J. L.; Li, J. H.; Liu, Y. B.; Cai, W. M.; Zhu, X. Y. Self-organized TiO_2 nanotube array sensor for the determination of chemical oxygen demand. *Adv. Mater.* **2008**, *20*, 1044–1049.

[6] Marichy, C.; Donato, N.; Willinger, M. G.; Latino, M.; Karpinsky, D.; Yu, S. H.; Neri, G.; Pinna, N. Tin dioxide sensing layer grown on tubular nanostructures by a non-

aqueous atomic layer deposition process. *Adv. Funct. Mater.* **2011**, *21*, 658–666.

[7] Liu, N.; Chen, X. Y.; Zhang, J. L.; Schwank, J. W. A review on TiO_2-based nanotubes synthesized via hydrothermal method: Formation mechanism, structure modification, and photocatalytic applications. *Catal. Today* **2014**, *225*, 34–51.

[8] Lee, C. H.; Xie, M.; Kayastha, V.; Wang, J. S.; Yap, Y. K. Patterned growth of boron nitride nanotubes by catalytic chemical vapor deposition. *Chem. Mater.* **2010**, *22*, 1782–1787.

[9] Métraux, C.; Grobéty, B. Tellurium nanotubes and nanorods synthesized by physical vapor deposition. *J. Mater. Res.* **2011**, *19*, 2159–2164.

[10] Lin, J.; Guo, M.; Yip, C. T.; Lu, W.; Zhang, G. G.; Liu, X. L.; Zhou, L. M.; Chen, X. F.; Huang, H. T. High temperature crystallization of free-standing anatase TiO_2 nanotube membranes for high efficiency dye-sensitized solar cells. *Adv. Funct. Mater.* **2013**, *23*, 5952–5960.

[11] Mohammadpour, A.; Waghmare, P. R.; Mitra, S. K.; Shankar, K. Anodic growth of large-diameter multipodal TiO_2 nanotubes. *ACS Nano* **2010**, *4*, 7421–7430.

[12] Miikkulainen, V.; Leskelä, M.; Ritala, M.; Puurunen, R. L. Crystallinity of inorganic films grown by atomic layer deposition: Overview and general trends. *J. Appl. Phys.* **2013**, *113*, 021301–021402.

[13] Marichy, C.; Bechelany, M.; Pinna, N. Atomic layer deposition of nanostructured materials for energy and environmental applications. *Adv. Mater.* **2012**, *24*, 1017–1032.

[14] Shin, H.; Jeong, D. K.; Lee, J.; Sung, M. M.; Kim, J. Formation of TiO_2 and ZrO_2 nanotubes using atomic layer deposition with ultraprecise control of the wall thickness. *Adv. Mater.* **2004**, *16*, 1197–1200.

[15] Peng, Q.; Sun, X. Y.; Spagnola, J. C.; Hyde, G. K.; Spontak, R. J.; Parsons, G. N. Atomic layer deposition on electrospun polymer fibers as a direct route to Al_2O_3 microtubes with precise wall thickness control. *Nano Lett.* **2007**, *7*, 719–722.

[16] Gu, D. F.; Baumgart, H.; Namkoong, G.; Abdel-Fattah, T. M. Atomic layer deposition of ZrO_2 and HfO_2 nanotubes by template replication. *Electrochem. Solid-State Lett.* **2009**, *12*, K25–K28.

[17] Qin, Y.; Vogelgesang, R.; Eßlinger, M.; Sigle, W.; van Aken, P. V.; Moutanabbir, O.; Knez, M. Bottom–up tailoring of plasmonic nanopeapods making use of the periodical topography of carbon nanocoil templates. *Adv. Funct. Mater.* **2012**, *22*, 5157–5165.

[18] Qin, Y.; Kim, Y.; Zhang, L. B.; Lee, S. M.; Yang, R. B.; Pan, A. L.; Mathwig, K.; Alexe, M.; Gösele, U.; Knez, M. Preparation and elastic properties of helical nanotubes obtained by atomic layer deposition with carbon nanocoils as templates. *Small* **2010**, *6*, 910–914.

[19] Ras, R. H. A.; Kemell, M.; de Wit, J.; Ritala, M.; ten Brinke, G.; Leskelä, M.; Ikkala, O. Hollow inorganic nanospheres and nanotubes with tunable wall thicknesses by atomic layer deposition on self-assembled polymeric templates. *Adv. Mater.* **2007**, *19*, 102–106.

[20] Wang, X. D.; Graugnard, E.; King, J. S.; Wang, Z. L.; Summers, C. J. Large-scale fabrication of ordered nanobowl arrays. *Nano Lett.* **2004**, *4*, 2223–2226.

[21] Peng, Q.; Sun, X. J.; Spagnola, J. C.; Saquing, C.; Khan, S. A.; Spontak, R. J.; Parsons, G. N. Bi-directional kirkendall effect in coaxial microtube nanolaminate assemblies fabricated by atomic layer deposition. *ACS Nano* **2009**, *3*, 546–554.

[22] Korhonen, J. T.; Hiekkataipale, P.; Malm, J.; Karppinen, M.; Ikkala, O.; Ras, R. H. A. Inorganic hollow nanotube aerogels by atomic layer deposition onto native nanocellulose templates. *ACS Nano* **2011**, *5*, 1967–1974.

[23] Li, F. B.; Yao, X. P.; Wang, Z. G.; Xing, W. H.; Jin, W. Q.; Huang, J.; Wang, Y. Highly porous metal oxide networks of interconnected nanotubes by atomic layer deposition. *Nano Lett.* **2012**, *12*, 5033–5038.

[24] Liu, K.; Sun, Y. H.; Liu, P.; Lin, X. Y.; Fan, S. S.; Jiang, K. L. Cross-stacked superaligned carbon nanotube films for transparent and stretchable conductors. *Adv. Funct. Mater.* **2011**, *21*, 2721–2728.

[25] Marichy, C.; Tessonnier, J. P.; Ferro, M. C.; Lee, K. H.; Schlögl, R.; Pinna, N.; Willinger, M. G. Labeling and monitoring the distribution of anchoring sites on functionalized CNTs by atomic layer deposition. *J. Mater. Chem.* **2012**, *22*, 7323–7330.

[26] Zhang, X. B.; Jiang, K. L.; Feng, C.; Liu, P.; Zhang, L. N.; Kong, J.; Zhang, T. H.; Li, Q. Q.; Fan, S. S. Spinning and processing continuous yarns from 4-inch wafer scale super-aligned carbon nanotube arrays. *Adv. Mater.* **2006**, *18*, 1505–1510.

[27] Puurunen, R. L.; Vandervorst, W. Island growth as a growth mode in atomic layer deposition: A phenomenological model. *J. Appl. Phys.* **2004**, *96*, 7686–7695.

[28] Farmer, D. B.; Gordon, R. G. Atomic layer deposition on suspended single-walled carbon nanotubes via gas-phase noncovalent functionalization. *Nano Lett.* **2006**, *6*, 699–703.

[29] Gomathi, A.; Vivekchand, S. R. C.; Govindaraj, A.; Rao, C. N. R. Chemically bonded ceramic oxide coatings on carbon nanotubes and inorganic nanowires. *Adv. Mater.* **2005**, *17*, 2757–2761.

[30] Willinger, M. G.; Neri, G.; Bonavita, A.; Micali, G.; Rauwel, E.; Herntrich, T.; Pinna, N. The controlled deposition of metal

oxides onto carbon nanotubes by atomic layer deposition: Examples and a case study on the application of V_2O_4 coated nanotubes in gas sensing. *Phys. Chem. Chem. Phys.* **2009**, *11*, 3615–3622.

[31] Willinger, M. G.; Neri, G.; Rauwel, E.; Bonavita A.; Micali, G.; Pinna, N. Vanadium oxide sensing layer grown on carbon nanotubes by a new atomic layer deposition process. *Nano Lett.* **2008**, *8*, 4201–4204.

[32] Meng, X. B.; Ionescu, M.; Banis, M. N.; Zhong, Y.; Liu, H.; Zhang, Y.; Sun, S. H.; Li, R. Y.; Sun, X. L. Heterostructural coaxial nanotubes of CNT@Fe_2O_3 via atomic layer deposition: Effects of surface functionalization and nitrogen-doping. *J. Nanopart. Res.* **2010**, *13*, 1207–1218.

[33] Kim, U. J.; Liu, X. M; Furtado, C. A.; Chen, G.; Saito, R.; Jiang, J.; Dresselhaus, M. S.; Eklund, P. C. Infrared-active vibrational modes of single-walled carbon nanotubes. *Phys. Rev. Lett.* **2005**, *95*, 157402–157406.

[34] Jiang, K. L.; Wang, J. P.; Li, Q. Q.; Liu, L.; Liu, C. H.; Fan, S. S. Superaligned carbon nanotube arrays, films, and yarns: A road to applications. *Adv. Mater.* **2011**, *23*, 1154–1161.

[35] Cheng, B. C.; Tian, B. X.; Xie, C. C.; Xiao, Y. H.; Lei, S. J. Highly sensitive humidity sensor based on amorphous Al_2O_3 nanotubes. *J. Mater. Chem.* **2011**, *21*, 1907–1912.

[36] Stere, C. E.; Adress, W.; Burch, R.; Chansai, S.; Goguet, A.; Graham, W. G.; De Rosa, F.; Palma, V.; Hardacre, C. Ambient temperature hydrocarbon selective catalytic reduction of NO_x using atmospheric pressure nonthermal plasma activation of a Ag/Al_2O_3 catalyst. *ACS Catal.* **2014**, *4*, 666–673.